International Journal of Heat and Mass Transfer 77 (2014) 717–729

Contents lists available at ScienceDirect

International Journal of Heat and Mass Transfer

journal homepage: www.elsevier.com/locate/ijhmt

Two-phase CO_2 migration in tilted aquifers in the presence of groundwater flow

Shujuan Wang [a], Kambiz Vafai [a,*], Sumit Mukhopadhyay [b]

[a] Department of Mechanical Engineering, University of California, Riverside, CA 92521, United States
[b] Earth Sciences Division, Lawrence Berkeley National Lab, Berkeley, CA 94720, United States

ARTICLE INFO

Article history:
Received 7 April 2014
Received in revised form 7 June 2014
Accepted 8 June 2014

Keywords:
Multiphase flow
Tilted aquifer
Groundwater flow
Porous media

ABSTRACT

A theoretical model for carbon dioxide (CO_2) migration in tilted aquifers with groundwater flow is presented to evaluate the injection of CO_2 into a geological formation. Capillary force in the flow of two immiscible fluids in a porous medium creates a saturation transition zone, where the saturation changes gradually. A vertical equilibrium assumption is employed to solve for the capillary pressure. Initially we verify our analytical model without slope and incoming ground water. Next the effects of sloped angle and an incoming ground water are studied. The asymmetrical distribution is fully incorporated in our analysis presented in this work, which provides essential information for CO_2 injection period and reservoir capacity. In the limiting case of no sloped stratum and no incoming groundwater flow as well as no transition zone, the results for our analysis compare very well with prior works. For the stratum with a slope angle, CO_2 will migrate further in the upper side of CO_2 injection point. The incoming underground water helps CO_2 move further on the up-dip side of the CO_2 injection point where CO_2 flow direction is the same as the incoming underground water. The existence of a critical velocity when the incoming CO_2 at the injection point will only move to the up-dip side is established. In this work, for the first time we account for the injection velocity and the saturation transition zone as well as a sloped incoming groundwater flow.

1. Introduction

Geological storage of CO_2 is a promising technology to reduce atmospheric CO_2 emissions (Bachu et al. [1]). In the Carbon capture and storage (CCS) process, CO_2 is captured, compressed and injected into a geological formation, such as a saline aquifer [1]. By understanding subsurface CO_2 migration, the stratum capacity and leakage risks of CO_2 storage can be estimated [2]. Theoretical models for CO_2 sequestration have been reviewed recently [2]. In this work, we present a theoretical model for CO_2 migration for tilted aquifers with groundwater flow. Reservoir capacity and migration process can be obtained utilizing the model presented here.

1.1. CO_2 storage in saline aquifer

Each year, gigatonnes of CO_2 need to be stored in the subsurface to reduce atmospheric CO_2 levels. As the saline aquifers have large potential volumetric storage capacity, they are currently the most promising target for CO_2 storage. Since the aquifer brine is not an accessible resource for drinking or irrigation due to its high concentrations of dissolved salts [3], CO_2 storage in it is unlikely to impact the quality of drinking water. Deep saline aquifers are located 1–3 km underneath the surface of the earth and consist of permeable material, such as limestone and cemented sand. Owing to formation movement, some aquifers are on a sloped strata and exposed to a slow moving groundwater flowing through it [2].

Before injection, CO_2 is compressed to reservoir conditions, at which the CO_2 is in a supercritical state, to save the storage volume. The injected CO_2 is the non-wetting phase and the groundwater is the wetting phase [4]. The compressed CO_2 is less dense and less viscous than the ground water. Buoyancy forces make CO_2 move upward until reaching the impermeable boundary overlying the aquifer formation. The injected CO_2 is structurally trapped by the impermeable layer and dominated by horizontal movement which is driven by the density difference with the groundwater. If the impermeable layer is not a closed structure and the caprock is not intact, long-term, the injected CO_2 could eventually leak. The long-term security is a major concern for the

* Corresponding author. Tel.: +1 9518272135; fax: +1 9518272899.
E-mail address: Vafai@ENGR.UCR.EDU (K. Vafai).

http://dx.doi.org/10.1016/j.ijheatmasstransfer.2014.06.019
0017-9310/

Nomenclature

ϕ	porosity
λ	mobility $Pa^{-1}*s^{-1}$
θ	slope angle
Q	flow rate [m^3/s]
q	groundwater surface flow rate [m^2/s]
U_w	groundwater incoming velocity [m/s]
s	effective non-wetting phase saturation
P_l	pressure change in the r direction [Pa]
S	saturation
S_{wi}	residual wetting phase saturation
h	the height of the non-wetting phase [m]
H	the height of the stratum [m]
μ	dynamic viscosity Pa*s
Λ	pore size distribution index
φ	coefficient defined as $\phi(1 - S_{wi})$
h_e	capillary entry height, $p_e/\Delta\rho g$ [m]
α	power for the non-wetting relative permeability equation
β	power for the wetting relative permeability equation
u	velocity vector [m/s]
Q_{well}	CO_2 Injection flow rate [m^3/s]
ε	very small parameter

Subscripts

R	up-dip
L	down-dip
r	relative
c	capillary
e	entrance
n	non-wetting phase
w	wetting phase

underground CO_2 storage. It mainly depends on the efficiency of the trapping mechanism. The long-term trapping mechanism can be divided into physical trapping and geochemical trapping [5]. In physical trapping, CO_2 is trapped by residual CO_2 saturation during imbibition or dissolved in the formation water. The geochemical trapping, which is also called mineral trapping, is the most permanent form of geological storage. The dissolved CO_2 forms ionic species and changes to stable carbonate minerals over long time scales after chemical reactions.

1.2. Interfacial model

CO_2 migration involves release of one fluid into another ambient fluid with a different density. One of the major difficulties in incorporating the intrusion of CO_2 in the stratum is modeling the interface between the intruding fluids and ambient fluids. To study such two-fluid systems through porous formations, sharp-interface models have often been invoked. The sharp-interface model assumes that each fluid in its region is fully saturated and two fluids are divided by a macroscopically sharp interface. Sharp-interface models are applicable when capillary forces are negligible compared to the other forces, such as viscous forces. Srinivsan and Vafai [6] utilized the sharp-interface model to analyze linear encroachment in two immiscible fluid systems in porous media and an analytical solution of the interface location was obtained. Their result was further improved by Vafai and Alazmi [7]. In confined geometries ($h \sim H$, h is the height of CO_2 in the aquifer, H is the thickness of the aquifer), where the viscosity ratio plays a key role, sharp-interface models are often adopted (Hesse et al. [2]). Nordbotten and Celia [8] obtained a symmetrical analytical solution incorporating the effects of vertical flow. Their model was applicable to gravity currents only when the capillary forces were negligible compared with other forces. However, when encountering two different phases, the saturation transition zone which is created by capillary forces is not negligible. The transition zone expands with the growth of capillary force compared with gravity, which is caused by the density difference between the two phases. This makes the sharp-interface assumption invalid. In this case, as CO_2 is injected into the brine system, the density difference between CO_2 and brine could potentially enlarge the transition zone. Golding et al. [4,9] derived a two-phase gravity-current model and considered the relative permeability reduction in the transition zone which was not included in a sharp-interface model. Nordbotten and Dahle [10] had shown that the capillary fringe had a potentially important impact on the of CO_2 migration plume shape and spread, both during the injection and post injection phases. The two-phase current model considering capillarity is adopted in this study.

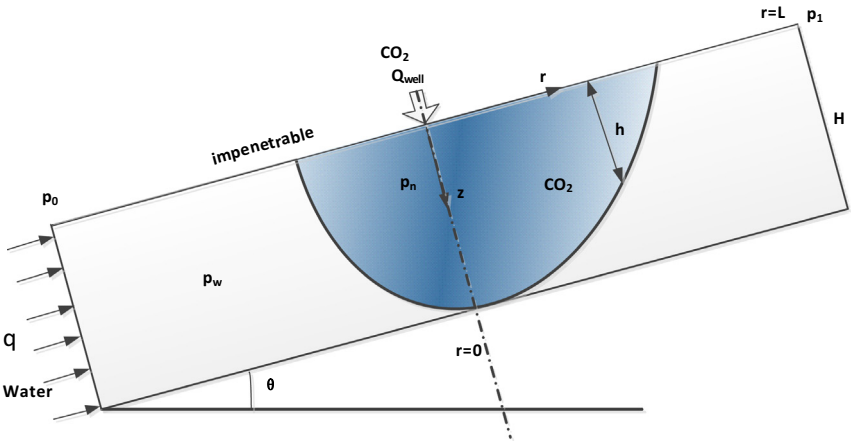

Fig. 1. Schematic diagram of a sloped stratum aquifer in the presence of groundwater flow.

Stratum is not always horizontal and often affects the flow of underground water for real CO_2 storage situations. In the present study, a plume of CO_2 is injected, as shown in Fig. 1, radially outward, from a vertical well into a tilted aquifer of uniform thickness and properties with a down-slope background flow. The co-injection of CO2 and water were discussed in Nordbotten and Celia's work [11]. The vertical well is located along the z coordinate axis as shown in Fig. 1 (The width of the well is neglected). The slope and underground water flow will impact the pressure distribution in the aquifer. In other words, it will affect the height distribution of CO_2 in the aquifer during the migration. Many studies of CO_2 storage have considered the sloped stratum and the flow of underground water. Hesse et al. [2] considered a slightly sloped aquifer, with an initial near-parabolic regime of CO_2. The slope of the aquifer accelerates the evolution of CO_2 regime from an initially near-parabolic shape to a near-hyperbolic shape. Macminn et al. [3] also presented a solution for CO_2 post-injection migration due to natural ground flow within a sloped aquifer. However, the surface tension or capillary force between CO_2 and ambient fluid in these models are neglected. In this study, capillary force is considered within CO_2 migration in the sloped stratum. Gravity-capillary equilibrium is assumed in the vertical direction. Nordbotten et al. [12] numerically analyzed the uncertainties of simulation of CO_2 storage in a slightly sloped aquifer. They considered the upscaling, and numerical modeling in their simulation. The importance of the real-time monitoring and history matching during injection operation was considered. Our study focuses on an analytical derivation and a comprehensive transient solution for the height evolution of non-wetting phase is obtained. For the first time, an analytical solution of CO_2 height distribution during the migration, which incorporates the injection velocity, incoming groundwater flow and the transition zone within a sloped aquifer, is established and presented.

2. Analysis of Two-phase CO_2 migration

2.1. Saturation and local mass conservation

In the injection process, the non-wetting fluid (CO_2) occupies the pores, which are initially saturated with the wetting fluid (ground water). In a two-phase model, the non-wetting fluid would just displace the wetting phase partially and the two phases co-exist within the same pore spaces [4]. The saturation, S_i is defined as the average volume fraction, ϕ_i, in a representative elementary volume (REV), normalized by porosity ϕ

$$S_i = \phi_i/\phi \quad i = w, n. \tag{1}$$

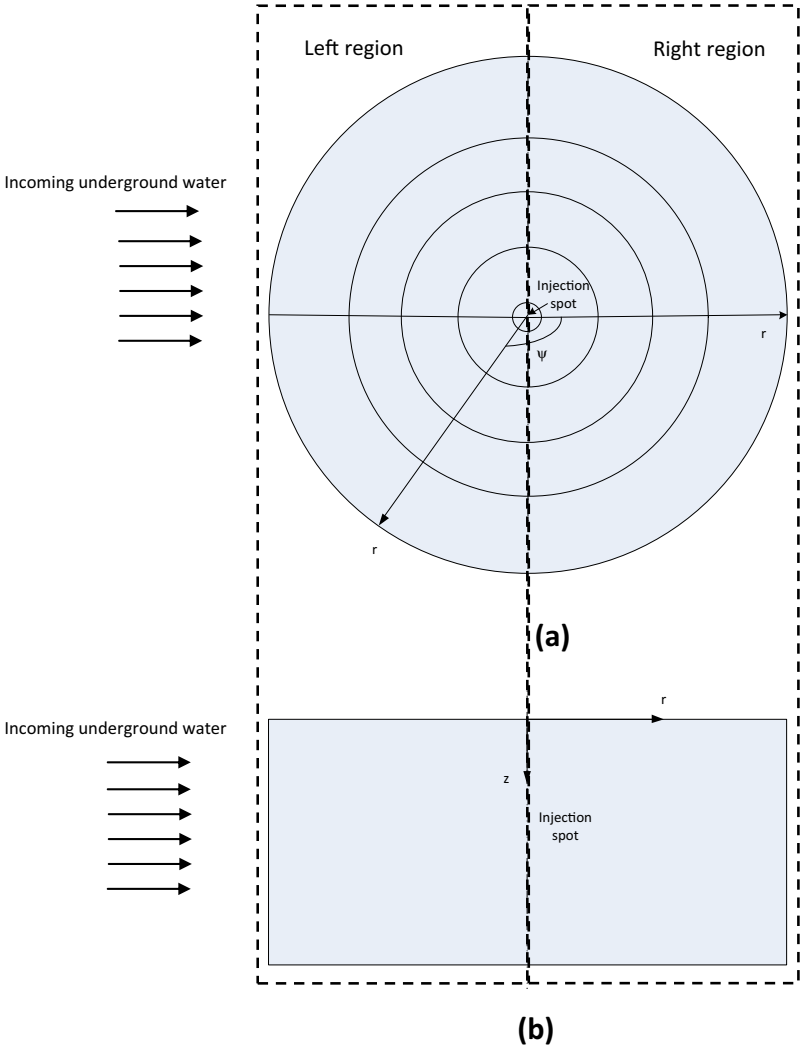

Fig. 2. The Sketch of the Injection Set-Up and the Coordinate System.

where w and n indicate wetting and non-wetting phases respectively. The methodology presented here partially follows that given by Golding et al. [4]. However here we extend it substantially to include the effects of formation slope and ambient groundwater flow and transient aspects because these could have significant influence on the extent of CO_2 migration and were not included in Golding et al. [4]. The effective non-wetting phase saturation s is defined by

$$s = \frac{S_n}{1 - S_{wr}} \tag{2}$$

where S_{wr} is the residual wetting phase saturation.

The local mass conservation equation for each phase in terms saturation is expressed as:

$$\phi \frac{\partial}{\partial t}(S_i) + \nabla \cdot \mathbf{u_i} = 0 \quad i = w, n \tag{3}$$

where $\mathbf{u}_i$ is the volumetric flux of phase i.

$h\,(r,t)$, as Fig. 1 shows, is the height of non-wetting phase. We assume that the non-wetting phase exists only in the region $0 < z < h(r,t)$. The non-wetting phase will not exist beyond this height.

As Fig. 1 shows, by using integration between $z = 0$ and h and using Leibniz integral rule, the local mass conservation equation in Cartesian coordinate system can be expressed as

$$\varphi \frac{\partial}{\partial t}\int_0^h s dz + \frac{\partial}{\partial x}\int_0^h u_n dz = 0 \tag{4}$$

where $\varphi = \phi(1 - S_{wr})$. In writing Eq. (4), we have assumed that the fluid phases are incompressible.

When injection ensues through a pipe, the migration occurs in all directions. As such the cylindrical coordinate is the proper and more realistic route to describe this physical process.

In cylindrical coordinate system, Eq. (4) will change to

$$\varphi \frac{\partial}{\partial t}\int_0^h s dz + \frac{1}{2\pi r}\frac{\partial}{\partial r}\left[2\pi r \int_0^h u_n dz\right] = 0 \tag{5}$$

Since there is incoming underground water flow, the height distribution is not symmetrical, with respect to the left and right sides of the injection site. Thus the asymmetrical nature of the flow needs to be considered in our case and Eq. (5) can't be directly used here. Here we first divide the migration region into two regions, as shown in Fig. 2, the left and the right side regions. As Fig. 2(b) shows, we utilize a 2D coordinate system, thus the height h we are solving for here is the average height over all angles ψ on the left or the right side for any specific radius r.

2.2. Capillary pressure

Capillary pressure is the pressure difference across the interface between two immiscible fluids, which is defined as

$$p_c = p_n - p_w \tag{6}$$

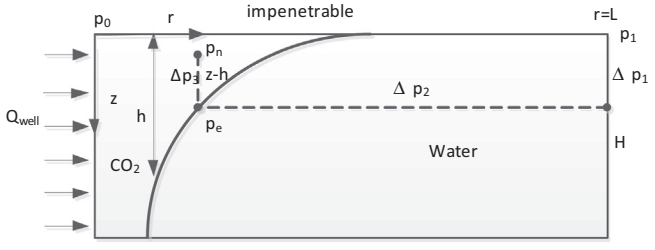

Fig. 3. Schematic of the configuration without the sloped stratum and incoming water flow.

Or expressed as

$$\frac{\partial p_c}{\partial z} = \frac{\partial p_n}{\partial z} - \frac{\partial p_w}{\partial z} \tag{7}$$

In the sharp-interface model, the capillary forces are neglected. During the injection period, the pores above the interface are filled with CO_2 and residual brine, while the brine fully occupies the pores below the interface [13]. When the capillary pressure is large, the sharp-interface assumption model becomes unrealistic. A capillary transition zone will develop under this condition. In the vertical direction, the fluid in the pores will gradually change from brine to CO_2 with residual brine in the transition zone. The thickness of the capillary transition zone is determined by the distribution of the capillary pressure.

Vertical gravity-capillary equilibrium assumption is employed to establish the capillary pressure distribution. It is valid when the vertical velocities are much less than the horizontal velocity. Since the aquifer length L is much greater than the height H, the vertical velocity can be neglected compared to the horizontal velocity and the pressure can be considered to be hydrostatic [4,9]. The pressure gradient for each phase can be expressed as

$$\frac{\partial p_n}{\partial z} = \rho_n g \cos\theta \quad \text{and} \quad \frac{\partial p_w}{\partial z} = \rho_w g \cos\theta \tag{8}$$

where θ is the angle of the sloped aquifer.

Thus the capillary force will balance with gravity in the vertical direction is given as

$$\frac{\partial p_c}{\partial z} = -\Delta\rho g \cos\theta \tag{9}$$

which is also called vertical gravity-capillary equilibrium, where $\Delta\rho = \rho_w - \rho_n$.

According to Brooks–Corey capillary pressure function [14], capillary pressure is a function of saturation, given by

$$p_c = p_e(1 - s)^{-1/\Lambda} \tag{10}$$

where Λ is the pore size distribution index. p_e is the capillary pressure at the boundary ($z = h$) of the non-wetting phase, which is defined as the required pressure for the non-wetting phase to enter the largest pores in the porous medium.

After integration, Eq. (9) can be presented as

$$p_c = p_e - \Delta\rho g(z - h)\cos\theta \tag{11}$$

By combining Eqs. (10) and (11), the non-wetting phase saturation s can be derived as

$$s[h(r,t),z] = 1 - \left(1 + \frac{h - z}{h_e}\cos\theta\right)^{-\Lambda} \tag{12}$$

where h_e is defined by capillary entry height $h_e = p_e/\Delta\,\rho g$.

2.3. Global mass conservation

2.3.1. Model without the slope and incoming groundwater flow

As Fig. 3 shows, the pressure in the CO_2 region p_n can be expressed as

$$\begin{aligned} p_n(r,z) &= p_1 + \Delta p_1 + \Delta p_2 + p_e + \Delta p_3 \\ &= p_1 + \rho_w g h + p_l + p_e - \rho_n g(h - z) \end{aligned} \tag{13}$$

At the boundary, there is a pressure jump p_e, which is the required pressure for the non-wetting phase to enter the largest pores in the porous medium. Define $p_l = \Delta p_2$, which is the pressure change in the r direction by the external pressure difference.

The pressure in groundwater region p_w can be expressed as

$$p_w(r,z) = p_0 + \rho_w g z + p_l \tag{14}$$

For two phase flow, the Darcy's law can be expressed as

$$u_i = -k\lambda_i\left(\frac{\partial p_i}{\partial r} - \rho_i g\right) \tag{15}$$

where λ_i is the mobility of each phase, $\lambda_i = k_{ri}(s)/\mu_i$ and k_{ri} is the relative permeability and μ_i is the dynamic viscosity, $i = n,w$.

We consider an incompressible and isothermal flow. Combining Darcy's law and the pressure equations, the velocity expression for each phase can be represented as

$$u_n = -k\lambda_n\left(\frac{\partial p_n}{\partial r}\right) = -k\lambda_n\left(\Delta\rho g\frac{\partial h}{\partial r} + \frac{\partial p_l}{\partial r}\right) \tag{16a}$$

$$u_w = -k\lambda_w\left(\frac{\partial p_w}{\partial r}\right) = -k\lambda_w\left(\frac{\partial p_l}{\partial r}\right) \tag{16b}$$

The relative permeability k_{ri} is commonly approximated as an exponential function of the effective saturation function s, given by

$$k_{rn} = k_{rn0}s^{\alpha} \tag{17a}$$

$$k_{rw} = (1-s)^{\beta} \tag{17b}$$

for non-wetting phase and wetting phases [15]. Experimental data obtained by Bennion and Bachu [16] for Ellerslie standstone shows that $\alpha = \beta = 2$ and $k_{rn0} = 0.116$. The same values were also used by Golding et al. [4] in their gravity current model. We employ these values in our work.

The flow rate for each phase can be expressed as

$$Q_n = 2\pi r\int_0^h u_n dz = 2\pi r\int_0^h -k\lambda_n\left(\Delta\rho g\frac{\partial h}{\partial r} + \frac{\partial p_l}{\partial r}\right)dz \tag{18a}$$

$$Q_w = 2\pi r\left(\int_0^h u_w dz + \int_h^H u_w dz\right) = 2\pi r\left(\int_0^h -k\lambda_w\left(\frac{\partial p_l}{\partial r}\right)dz - (H-h)\lambda'_w\left(\frac{\partial p_l}{\partial r}\right)\right) \tag{18b}$$

where H is the height of the stratum, $\lambda'_w = \frac{k_{rw}}{\mu_w} = \frac{1}{\mu_w}$. For the groundwater region, $k_{rw} = 1$.

Combined with (17a,b), the corresponding flow rates can be expressed as

$$Q_n = -2\pi r\left(\Delta\rho g\frac{\partial h}{\partial r} + \frac{\partial p_l}{\partial r}\right)\frac{kk_{rn0}}{\mu_n}\int_0^h s^{\alpha}dz \tag{19a}$$

$$Q_w = -2\pi r\left(\frac{\partial p_l}{\partial r}\right)\frac{k}{\mu_w}\left(\int_0^h (1-s)^{\beta}dz + (H-h)\right) \tag{19b}$$

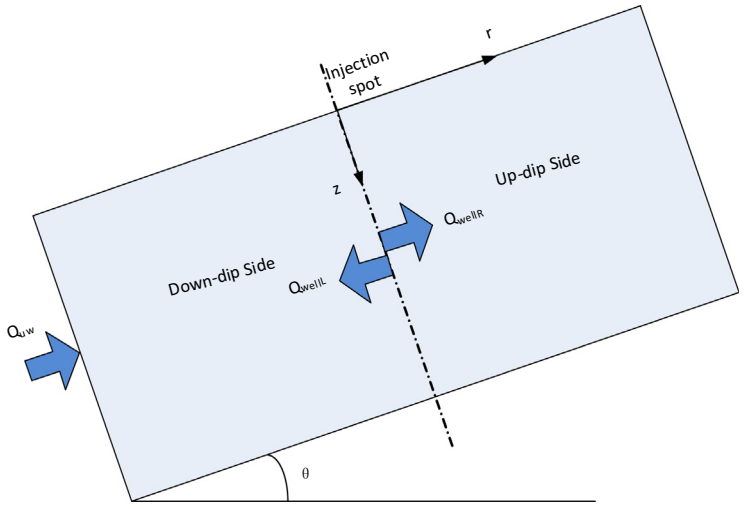

(a)

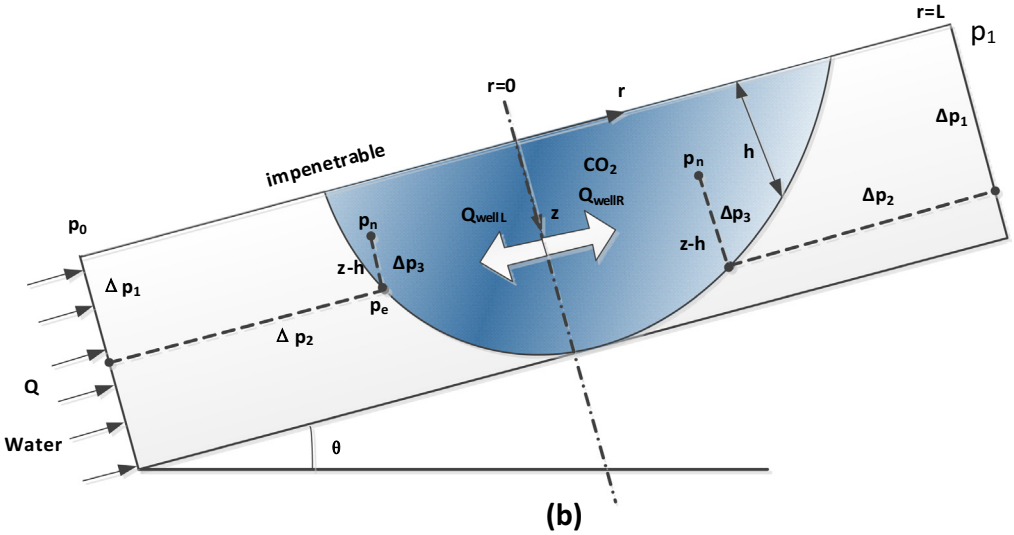

(b)

Fig. 4. Pressure Distribution on the two sides of the injection site.

Two integrations, $\int_0^h s^\alpha dz$ and $\int_0^h (1-s)^\beta dz$, in the case of $\alpha = \beta = 2$, combined with Eq. (12), can be expressed as

$$\int_0^h s^\alpha dz = h_e\left(\frac{h}{h_e} + \frac{2}{\Lambda-1}\left(1+\frac{h}{h_e}\right)^{-\Lambda+1} - \frac{2}{\Lambda-1} - \frac{1}{2\Lambda-1}\left(1+\frac{h}{h_e}\right)^{-2\Lambda+1} + \frac{1}{2\Lambda-1}\right) \tag{20a}$$

$$\int_0^h (1-s)^\beta dz = -h_e\left(\frac{1}{2\Lambda-1}\left(1+\frac{h}{h_e}\right)^{-2\Lambda+1} - \frac{1}{2\Lambda-1}\right) \tag{20b}$$

Substituting (20a,b) into (19a,b), and using global mass conservation equation

$$Q_n + Q_w = Q_{well} \tag{21}$$

yields

$$\frac{\partial p_l}{\partial r} = -\frac{Q_{well} + 2\pi r\Delta\rho g\frac{\partial h}{\partial r}\frac{kk_{rn0}}{\mu_n}F}{2\pi r\frac{k}{\mu_w}E + 2\pi r\frac{kk_{rn0}}{\mu_n}F} \tag{22}$$

where Q_{well} is the injection flow rate of CO_2. As Fig. 1 shows, the well location is along the z coordinate axis and it spans the depth of the aquifer.

$$E = -h_e\left(\frac{1}{2\Lambda-1}\left(1+\frac{h}{h_e}\right)^{-2\Lambda+1} - \frac{1}{2\Lambda-1}\right) + (H-h),$$

$$F = h_e\left(\frac{h}{h_e} + \frac{2}{\Lambda-1}\left(1+\frac{h}{h_e}\right)^{-\Lambda+1} - \frac{2}{\Lambda-1} - \frac{1}{2\Lambda-1}\left(1+\frac{h}{h_e}\right)^{-2\Lambda+1} + \frac{1}{2\Lambda-1}\right).$$

Combining Eqs. (5), (12), (16a), (20a) and (22), yields

$$\varphi\left[1-\left(1+\frac{h}{h_e}\right)^{-\Lambda}\right]\frac{\partial h}{\partial t} - \frac{kk_{rn0}}{\mu_n}\frac{1}{2\pi r}\frac{\partial}{\partial r} \times\left\{2\pi rF\left[\Delta\rho g\frac{\partial h}{\partial r} - \frac{Q_{well}+2\pi r\Delta\rho g\frac{\partial h}{\partial r}\frac{kk_{rn0}}{\mu_n}F}{2\pi r\frac{k}{\mu_w}E + 2\pi r\frac{kk_{rn0}}{\mu_n}F}\right]\right\} = 0 \tag{23}$$

Compared with the transport in the matrix of aquifer, CO_2 can quickly fill up the well without resistance from the porous media. As the well spans the depth H of the aquifer, the boundary conditions for Eq. (23) are $h|_{r=0} = H$, $h|_{r=L} = h_0$ where h_0 is the initial height. The initial height h_0 allows for a more general case of some existing CO_2 in the aquifer before the injection. And the length of the aquifer is large enough that we can assume CO_2 height at $r = L$ equals to the initial height.

2.3.2. Model with the slope and incoming groundwater flow

As shown in Fig. 4(a) when considering the slope and the incoming groundwater flow, the injected CO_2 can be divided into two parts Q_{wellR} and Q_{wellL}. Q_{wellR} is the component which is in the same direction as the incoming ground flow while The direction of Q_{wellL} is in the opposite direction. Due to the slope and the incoming groundwater flow, the height distribution on the up-dip and the down-dip regions are asymmetrical and need to be considered separately. This asymmetry is caused by the effect of gravity and incoming underground water flow and is fully incorporated in our analysis. As we have mentioned earlier, a 2D coordinate system is utilized and the height h which is obtained here is the average height over all angles ψ on the left or the right side for any specific radius r.

As shown in Fig. 4(b), on the up-dip side region, the pressure in CO_2 region p_n can be expressed as

$$\begin{aligned} p_n(r,z) &= p_1 + \Delta p_1 + \Delta p_2 + p_e + \Delta p_3 \\ &= p_0 + \rho_w g h\cos\theta + p_l + p_e - \rho_n g(h-z)\cos\theta \end{aligned} \tag{24}$$

and the pressure in the groundwater region p_w can be expressed as

$$p_w(r,z) = p_1 + \rho_w g z\cos\theta + p_l \tag{25}$$

Thus the flow rate on the up-dip side region for each phase can be expressed as

$$Q_n = -\pi r\left(\Delta\rho g\cos\theta\frac{\partial h}{\partial r} + \frac{\partial p_l}{\partial r} + \rho_n g\sin\theta\right)\frac{kk_{rn0}}{\mu_n}\int_0^h s^\alpha dz \tag{26a}$$

$$Q_w = -\pi r\left(\frac{\partial p_l}{\partial r} + \rho_w g\sin\theta\right)\frac{k}{\mu_w}\left(\int_0^h (1-s)^\beta dz + (H-h)\right) \tag{26b}$$

where

$$\int_0^h s^\alpha dz = \frac{h_e}{\cos\theta}\left(\frac{h\cos\theta}{h_e} + \frac{2}{\Lambda-1}\left(1+\frac{h\cos\theta}{h_e}\right)^{-\Lambda+1} - \frac{2}{\Lambda-1} - \frac{1}{2\Lambda-1}\left(1+\frac{h\cos\theta}{h_e}\right)^{-2\Lambda+1} + \frac{1}{2\Lambda-1}\right) \tag{27a}$$

$$\int_0^h (1-s)^\beta dz = -\frac{h_e}{\cos\theta}\left(\frac{1}{2\Lambda-1}\left(1+\frac{h\cos\theta}{h_e}\right)^{-2\Lambda+1} - \frac{1}{2\Lambda-1}\right) \tag{27b}$$

The incoming groundwater flow rate can be expressed as

$$q = U_w H \tag{28}$$

U_w is the incoming groundwater flow velocity.

Considering the incoming groundwater flow, the global mass conservation in the $r > 0$ region can be expressed as

$$Q_n + Q_w = Q_{wellR} + 2rq \tag{29}$$

Combining Eqs. (26a,b), (27a,b) and (29), we can obtain an expression for $\frac{\partial p_l}{\partial r}$

$$\frac{\partial p_l}{\partial r} = -\frac{1}{\pi r\frac{k}{\mu_w}\left[-\frac{h_e}{\cos\theta}\left(\frac{1}{2\Lambda-1}\left(1+\frac{h\cos\theta}{h_e}\right)^{-2\Lambda+1} - \frac{1}{2\Lambda-1}\right) + (H-h)\right] + \pi r\frac{kk_{rn0}}{\mu_n}\frac{h_e}{\cos\theta}\left(\frac{h\cos\theta}{h_e} + \frac{2}{\Lambda-1}\left(1+\frac{h\cos\theta}{h_e}\right)^{-\Lambda+1} - \frac{2}{\Lambda-1} - \frac{1}{2\Lambda-1}\left(1+\frac{h\cos\theta}{h_e}\right)^{-2\Lambda+1} + \frac{1}{2\Lambda-1}\right)}$$

$$\left\{\begin{array}{l} Q_{wellR} + 2rq + \pi r\left(\Delta\rho g\cos\theta\frac{\partial h}{\partial r} + \rho_n g\sin\theta\right)\frac{kk_{rn0}}{\mu_n}\frac{h_e}{\cos\theta}\left(\frac{h\cos\theta}{h_e} + \frac{2}{\Lambda-1}\left(1+\frac{h\cos\theta}{h_e}\right)^{-\Lambda+1} - \frac{2}{\Lambda-1} - \frac{1}{2\Lambda-1}\left(1+\frac{h\cos\theta}{h_e}\right)^{-2\Lambda+1} + \frac{1}{2\Lambda-1}\right) \\ +\pi r\rho_w g\sin\theta\frac{k}{\mu_w}\left[-\frac{h_e}{\cos\theta}\left(\frac{1}{2\Lambda-1}\left(1+\frac{h\cos\theta}{h_e}\right)^{-2\Lambda+1} - \frac{1}{2\Lambda-1}\right) + (H-h)\right] \end{array}\right\} \tag{30}$$

Combining Eqs. (5), (12), (26a), (27a) and (30), we obtain the following governing equation for the height h.

$$\varphi\left[1-\left(1+\frac{h}{h_e}\cos\theta\right)^{-\Lambda}\right]\frac{\partial h}{\partial t}-\frac{kk_{rn0}}{\mu_n}\frac{1}{\pi r}\frac{\partial}{\partial r}\left\{\pi r\left[\begin{array}{l}\Delta\rho g\cos\theta\frac{\partial h}{\partial r}+\rho_n g\sin\theta\\ -\frac{1}{\pi r\frac{k}{\mu_w}\left[-\frac{h_e}{\cos\theta}\left(\frac{1}{2\Lambda-1}\left(1+\frac{h\cos\theta}{h_e}\right)^{-2\Lambda+1}-\frac{1}{2\Lambda-1}\right)+(H-h)\right]+\pi r\frac{kk_{rn0}}{\mu_n}\frac{h_e}{\cos\theta}\left(\frac{h\cos\theta}{h_e}+\frac{2}{\Lambda-1}\left(1+\frac{h\cos\theta}{h_e}\right)^{-\Lambda+1}-\frac{2}{\Lambda-1}-\frac{1}{2\Lambda-1}\left(1+\frac{h\cos\theta}{h_e}\right)^{-2\Lambda+1}+\frac{1}{2\Lambda-1}\right)}\\ \left\{\begin{array}{l}Q_{wellR}+2rq+\pi r\left(\Delta\rho g\cos\theta\frac{\partial h}{\partial r}+\rho_n g\sin\theta\right)\frac{kk_{rn0}}{\mu_n}\frac{h_e}{\cos\theta}\left(\frac{h\cos\theta}{h_e}+\frac{2}{\Lambda-1}\left(1+\frac{h\cos\theta}{h_e}\right)^{-\Lambda+1}\right.\\ \left.-\frac{2}{\Lambda-1}-\frac{1}{2\Lambda-1}\left(1+\frac{h\cos\theta}{h_e}\right)^{-2\Lambda+1}+\frac{1}{2\Lambda-1}\right)\\ +\pi r\rho_w g\sin\theta\frac{k}{\mu_w}\left[-\frac{h_e}{\cos\theta}\left(\frac{1}{2\Lambda-1}\left(1+\frac{h\cos\theta}{h_e}\right)^{-2\Lambda+1}-\frac{1}{2\Lambda-1}\right)+(H-h)\right]\end{array}\right]\\ \frac{h_e}{\cos\theta}\left(\frac{h\cos\theta}{h_e}+\frac{2}{\Lambda-1}\left(1+\frac{h\cos\theta}{h_e}\right)^{-\Lambda+1}-\frac{2}{\Lambda-1}-\frac{1}{2\Lambda-1}\left(1+\frac{h\cos\theta}{h_e}\right)^{-2\Lambda+1}+\frac{1}{2\Lambda-1}\right)\end{array}\right\}=0 \tag{31}$$

On down-dip side region, the pressure in the CO_2 region p_n can be expressed as

$$\begin{aligned}p_n(r,z)&=p_0+\Delta p_1+\Delta p_2+p_e+\Delta p_3\\&=p_0+\rho_w gh\cos\theta+p_l+p_e-\rho_n g(h-z)\cos\theta\end{aligned} \tag{32}$$

The global mass conservation on the down-dip side region is

$$Q_n+Q_w=Q_{wellL}-2rq \tag{33}$$

Q_{wellL} is the CO_2 flow rate on the down-dip side and

$$Q_n=-\pi r\left(\Delta\rho g\cos\theta\frac{\partial h}{\partial r}+\frac{\partial p_l}{\partial r}-\rho_n g\sin\theta\right)\frac{kk_{rn0}}{\mu_n}\int_0^h s^\alpha dz \tag{34a}$$

$$Q_w=-\pi r\left(\frac{\partial p_l}{\partial r}-\rho_w g\sin\theta\right)\frac{k}{\mu_w}\left(\int_0^h(1-s)^\beta dz+(H-h)\right) \tag{34b}$$

As such, the governing equation for the height distribution can be expressed as

The CO_2 flow rate on the up-dip side Q_{wellR} and the down-dip side Q_{wellL} will satisfy the following equation

$$Q_{wellR}+Q_{wellL}=Q_{well} \tag{36}$$

If the impact of slope and incoming flow ground water on the injection of CO_2 can be neglected, the flow rate on the up-dip side will equal that on the down-dip side.

$$Q_{wellR}=Q_{wellL}=Q_{well}/2 \tag{37}$$

As the injection period lasts for several years and the injected CO_2 would migrate thousands of meters, Eqs. (23), (31) and (35) need to be rewritten in a dimensionless form. Eqs. (38)–(40) are the dimensionless forms of Eqs. (23), (31) and (35) respectively.

$$\varphi\left[1-\left(1+\frac{h}{h_e}\cos\theta\right)^{-\Lambda}\right]\frac{\partial h}{\partial t}-\frac{kk_{rn0}}{\mu_n}\frac{1}{\pi r}\frac{\partial}{\partial r}\left\{\pi r\left[\begin{array}{l}\Delta\rho g\cos\theta\frac{\partial h}{\partial r}-\rho_n g\sin\theta\\ -\frac{1}{\pi r\frac{k}{\mu_w}\left[-\frac{h_e}{\cos\theta}\left(\frac{1}{2\Lambda-1}\left(1+\frac{h\cos\theta}{h_e}\right)^{-2\Lambda+1}-\frac{1}{2\Lambda-1}\right)+(H-h)\right]+\pi r\frac{kk_{rn0}}{\mu_n}\frac{h_e}{\cos\theta}\left(\frac{h\cos\theta}{h_e}+\frac{2}{\Lambda-1}\left(1+\frac{h\cos\theta}{h_e}\right)^{-\Lambda+1}-\frac{2}{\Lambda-1}-\frac{1}{2\Lambda-1}\left(1+\frac{h\cos\theta}{h_e}\right)^{-2\Lambda+1}+\frac{1}{2\Lambda-1}\right)}\\ \left\{\begin{array}{l}Q_{wellL}-2rq+\pi r\left(\Delta\rho g\cos\theta\frac{\partial h}{\partial r}-\rho_n g\sin\theta\right)\frac{kk_{rn0}}{\mu_n}\frac{h_e}{\cos\theta}\left(\frac{h\cos\theta}{h_e}+\frac{2}{\Lambda-1}\left(1+\frac{h\cos\theta}{h_e}\right)^{-\Lambda+1}-\frac{2}{\Lambda-1}-\frac{1}{2\Lambda-1}\left(1+\frac{h\cos\theta}{h_e}\right)^{-2\Lambda+1}+\frac{1}{2\Lambda-1}\right)\\ -\pi r\rho_w g\sin\theta\frac{k}{\mu_w}\left[-\frac{h_e}{\cos\theta}\left(\frac{1}{2\Lambda-1}\left(1+\frac{h\cos\theta}{h_e}\right)^{-2\Lambda+1}-\frac{1}{2\Lambda-1}\right)+(H-h)\right]\end{array}\right\}\\ \frac{h_e}{\cos\theta}\left(\frac{h\cos\theta}{h_e}+\frac{2}{\Lambda-1}\left(1+\frac{h\cos\theta}{h_e}\right)^{-\Lambda+1}-\frac{2}{\Lambda-1}-\frac{1}{2\Lambda-1}\left(1+\frac{h\cos\theta}{h_e}\right)^{-2\Lambda+1}+\frac{1}{2\Lambda-1}\right)\end{array}\right\}=0 \tag{35}$$

$$\varphi\left[1-(1+\tfrac{h'}{h_e/H})^{-\Lambda}\right]\tfrac{\partial h'}{\partial t'}-\tfrac{T}{H}\,\tfrac{kk_{rn0}}{\mu_n}\,\tfrac{H^2}{L^2}\,\tfrac{1}{2\pi r'}$$
$$\frac{\partial}{\partial r'}\left\{\begin{array}{l} 2\pi r'\left[\begin{array}{l}\Delta\rho g\,\frac{\partial h'}{\partial r'}-\\ \dfrac{Q_{well}/H+2\pi r'\Delta\rho g\frac{\partial h'}{\partial r'}\frac{kk_{rn0}}{\mu_n}h_e\left(\frac{h'}{h_e/H}+\frac{2}{\Lambda-1}\left(1+\frac{h'}{h_e/H}\right)^{-\Lambda+1}-\frac{2}{\Lambda-1}-\frac{1}{2\Lambda-1}\left(1+\frac{h'}{h_e/H}\right)^{-2\Lambda+1}+\frac{1}{2\Lambda-1}\right)}{2\pi r'\frac{kH}{\mu_w}\left[-\frac{h_e}{H}\left(\frac{1}{2\Lambda-1}\right)^{-2\Lambda+1}-\frac{1}{2\Lambda-1})+(1-h'))\right]+2\pi r'\frac{kk_{rn0}}{\mu_n}h_e\left(\frac{h'}{h_e/H}+\frac{2}{\Lambda-1}\left(1+\frac{h'}{h_e/H}\right)^{-\Lambda+1}-\frac{2}{\Lambda-1}-\frac{1}{2\Lambda-1}\left(1+\frac{h'}{h_e/H}\right)^{-2\Lambda+1}+\frac{1}{2\Lambda-1}\right)}\end{array}\right]\\ \frac{h_e}{H}\left(\frac{h'}{h_e/H}+\frac{2}{\Lambda-1}\left(1+\frac{h'}{h_e/H}\right)^{-\Lambda+1}-\frac{2}{\Lambda-1}-\frac{1}{2\Lambda-1}\left(1+\frac{h'}{h_e/H}\right)^{-2\Lambda+1}+\frac{1}{2\Lambda-1}\right)\end{array}\right\}$$
$$=0 \tag{38}$$

$$\varphi\left[1-(1+\tfrac{h'}{h_e/H}\cos\theta)^{-\Lambda}\right]\tfrac{\partial h'}{\partial t'}-\tfrac{T}{H}\tfrac{kk_{rn0}}{\mu_n}\tfrac{H^2}{L^2}\tfrac{1}{\pi r'}$$
$$\frac{\partial}{\partial r'}\left\{\begin{array}{l}\pi r'\left[\begin{array}{l}\Delta\rho g\cos\theta\frac{\partial h'}{\partial r'}+\rho_n g\sin\theta\frac{L}{H}\\ -\dfrac{1}{\pi r'\frac{kH}{\mu_w}\left[-\frac{h_e}{H\cos\theta}\left(\frac{1}{2\Lambda-1}(1+\frac{h'\cos\theta}{h_e/H})^{-2\Lambda+1}-\frac{1}{2\Lambda-1}\right)+(1-h')\right]+\pi r'\frac{kk_{rn0}}{\mu_n}\frac{h_e}{\cos\theta}\left(\frac{h'\cos\theta}{h_e/H}+\frac{2}{\Lambda-1}\left(1+\frac{h'\cos\theta}{h_e/H}\right)^{-\Lambda+1}-\frac{2}{\Lambda-1}-\frac{1}{2\Lambda-1}\left(1+\frac{h'\cos\theta}{h_e/H}\right)^{-2\Lambda+1}+\frac{1}{2\Lambda-1}\right)}\\ \left\{\begin{array}{l}Q_{wellR}/H+2r'q\frac{L}{H}+\pi r'\left(\Delta\rho g\cos\theta\frac{\partial h'}{\partial r'}+\rho_n g\sin\theta\frac{L}{H}\right)\frac{kk_{rn0}}{\mu_n}\frac{h_e}{\cos\theta}\left(\frac{h'\cos\theta}{h_e/H}+\frac{2}{\Lambda-1}\left(1+\frac{h'\cos\theta}{h_e/H}\right)^{-\Lambda+1}-\frac{2}{\Lambda-1}-\frac{1}{2\Lambda-1}\left(1+\frac{h'\cos\theta}{h_e/H}\right)^{-2\Lambda+1}+\frac{1}{2\Lambda-1}\right)\\ +\pi r'\rho_w g\sin\theta\frac{L}{H}\frac{kH}{\mu_w}\left[-\frac{h_e}{H\cos\theta}\left(\frac{1}{2\Lambda-1}(1+\frac{h'\cos\theta}{h_e/H})^{-2\Lambda+1}-\frac{1}{2\Lambda-1}\right)+(1-h')\right]\end{array}\right\}\end{array}\right]\\ \frac{h_e}{H\cos\theta}\left(\frac{h'\cos\theta}{h_e/H}+\frac{2}{\Lambda-1}\left(1+\frac{h'\cos\theta}{h_e/H}\right)^{-\Lambda+1}-\frac{2}{\Lambda-1}-\frac{1}{2\Lambda-1}\left(1+\frac{h'\cos\theta}{h_e/H}\right)^{-2\Lambda+1}+\frac{1}{2\Lambda-1}\right)\end{array}\right\}=0 \tag{39}$$

$$\varphi\left[1-(1+\tfrac{h'}{h_e/H}\cos\theta)^{-\Lambda}\right]\tfrac{\partial h'}{\partial t'}-\tfrac{T}{H}\tfrac{kk_{rn0}}{\mu_n}\tfrac{H^2}{L^2}\tfrac{1}{\pi r'}$$
$$\frac{\partial}{\partial r'}\left\{\begin{array}{l}\pi r'\left[\begin{array}{l}\Delta\rho g\cos\theta\frac{\partial h'}{\partial r'}-\rho_n g\sin\theta\frac{L}{H}\\ -\dfrac{1}{\pi r'\frac{kH}{\mu_w}\left[-\frac{h_e}{H\cos\theta}\left(\frac{1}{2\Lambda-1}(1+\frac{h'\cos\theta}{h_e/H})^{-2\Lambda+1}-\frac{1}{2\Lambda-1}\right)+(1-h')\right]+\pi r'\frac{kk_{rn0}}{\mu_n}\frac{h_e}{\cos\theta}\left(\frac{h'\cos\theta}{h_e/H}+\frac{2}{\Lambda-1}\left(1+\frac{h'\cos\theta}{h_e/H}\right)^{-\Lambda+1}-\frac{2}{\Lambda-1}-\frac{1}{2\Lambda-1}\left(1+\frac{h'\cos\theta}{h_e/H}\right)^{-2\Lambda+1}+\frac{1}{2\Lambda-1}\right)}\\ \left\{\begin{array}{l}Q_{wellR}/H-2r'q\frac{L}{H}+\pi r'\left(\Delta\rho g\cos\theta\frac{\partial h'}{\partial r'}-\rho_n g\sin\theta\frac{L}{H}\right)\frac{kk_{rn0}}{\mu_n}\frac{h_e}{\cos\theta}\left(\frac{h'\cos\theta}{h_e/H}+\frac{2}{\Lambda-1}\left(1+\frac{h'\cos\theta}{h_e/H}\right)^{-\Lambda+1}-\frac{2}{\Lambda-1}-\frac{1}{2\Lambda-1}\left(1+\frac{h'\cos\theta}{h_e/H}\right)^{-2\Lambda+1}+\frac{1}{2\Lambda-1}\right)\\ -\pi r'\rho_w g\sin\theta\frac{L}{H}\frac{kH}{\mu_w}\left[-\frac{h_e}{H\cos\theta}\left(\frac{1}{2\Lambda-1}(1+\frac{h'\cos\theta}{h_e/H})^{-2\Lambda+1}-\frac{1}{2\Lambda-1}\right)+(1-h')\right]\end{array}\right\}\end{array}\right]\\ \frac{h_e}{H\cos\theta}\left(\frac{h'\cos\theta}{h_e/H}+\frac{2}{\Lambda-1}\left(1+\frac{h'\cos\theta}{h_e/H}\right)^{-\Lambda+1}-\frac{2}{\Lambda-1}-\frac{1}{2\Lambda-1}\left(1+\frac{h'\cos\theta}{h_e/H}\right)^{-2\Lambda+1}+\frac{1}{2\Lambda-1}\right)\end{array}\right\}=0 \tag{40}$$

In these equations the characteristic length scale H is chosen to be the thickness of the aquifer. Since the width of the aquifer is much larger than its thickness, the characteristic radius L is chosen to be 100 times the aquifer thickness H. Also since the duration of CO_2 injection lasts for several years, the characteristic time scale T is chosen to be 1 year. The dimensionless boundary conditions can be represented by $h'|_{r'=0}=1$, $h'|_{r'=1}=h_0/H$.

Introducing

$$A=\frac{H}{\mu_w}\left[-\frac{h_e}{H\cos\theta}\left(\frac{1}{2\Lambda-1}\left(1+\frac{h'\cos\theta}{h_e/H}\right)^{-2\Lambda+1}-\frac{1}{2\Lambda-1}\right)+(1-h')\right] \tag{41}$$

$$B=\frac{k_{rn0}}{\mu_n}\frac{h_e}{\cos\theta}\left(\frac{h'\cos\theta}{h_e/H}+\frac{2}{\Lambda-1}\left(1+\frac{h'\cos\theta}{h_e/H}\right)^{-\Lambda+1}\right.$$
$$\left.-\frac{2}{\Lambda-1}-\frac{1}{2\Lambda-1}\left(1+\frac{h'\cos\theta}{h_e/H}\right)^{-2\Lambda+1}+\frac{1}{2\Lambda-1}\right) \tag{42}$$

Table 1
Parametric values used in comparisons with prior work [8,15].

Parameter	Value
Porosity ϕ	0.15
Residual wetting phase saturationS_{wi}	0.2
Ground water density ρ_w	1000 kg/m^3
CO_2 density ρ_n	733 kg/m^3
Enter pressure p_e	3000 Pa
Permeability k	1E-13m^2
CO_2 viscosity	0.00006 Pa∗s
Ground water viscosity	0.0005 Pa∗s
Pore size distribution index Λ	2
Groundwater incoming velocity U_w	1 feet/day (3.53E−7 m/s)
CO_2 Injection flow rate Q_{well}	0.0439 m^3/s
Capillary entry height h_e	1.147 m
Aquifer thickness H	100 m
Characteristic radius L	10,000 m
Initial CO_2 thickness h_0	10 m

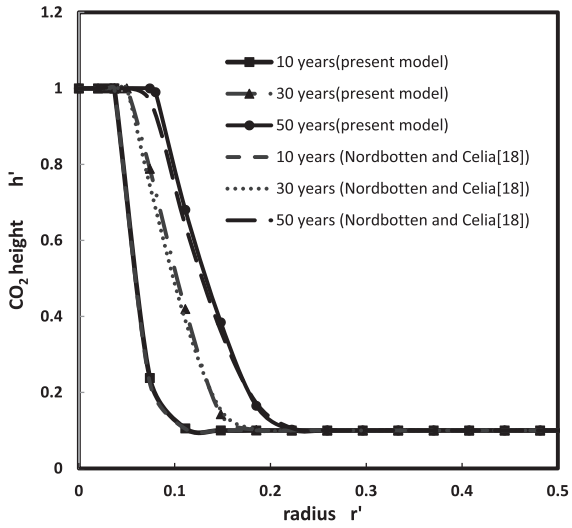

Fig. 5. The height distribution for the limiting case without the sloped stratum and incoming groundwater flow-comparison between the present work and Nordbotten and Celia [18].

Eqs. (39) and (40) can be simplified to

$$\varphi\left[1-\left(1+\frac{h'}{h_e/H}\cos\theta\right)^{-\Lambda}\right]\frac{\partial h'}{\partial t'}-\frac{T}{H}\frac{kk_{rn0}}{\mu_n}\frac{H^2}{L^2}\frac{1}{r'}\frac{h_e}{H\cos\theta}\frac{\partial}{\partial r'}\left\{\begin{array}{l}\left[\Delta\rho g\cos\theta r'\frac{\partial h'}{\partial r'}\frac{A}{A+B}-\Delta\rho g\sin\theta r'\frac{L}{H}\frac{A}{A+B}-\frac{1}{A+B}\frac{(Q_{wellR}+2qLr)}{\pi Hk}\right]\\ \left(\frac{h'\cos\theta}{h_e/H}+\frac{2}{\Lambda-1}\left(1+\frac{h'\cos\theta}{h_e/H}\right)^{-\Lambda+1}-\frac{2}{\Lambda-1}-\frac{1}{2\Lambda-1}\left(1+\frac{h'\cos\theta}{h_e/H}\right)^{-2\Lambda+1}+\frac{1}{2\Lambda-1}\right)\end{array}\right\}=0 \quad (43)$$

$$\varphi\left[1-\left(1+\frac{h'}{h_e/H}\cos\theta\right)^{-\Lambda}\right]\frac{\partial h'}{\partial t'}-\frac{T}{H}\frac{kk_{rn0}}{\mu_n}\frac{H^2}{L^2}\frac{1}{r'}\frac{h_e}{H\cos\theta}\frac{\partial}{\partial r'}\left\{\begin{array}{l}\left[\Delta\rho g\cos\theta r'\frac{\partial h'}{\partial r'}\frac{A}{A+B}+\Delta\rho g\sin\theta r'\frac{L}{H}\frac{A}{A+B}-\frac{1}{A+B}\frac{(Q_{wellL}-2qLr)}{\pi Hk}\right]\\ \left(\frac{h'\cos\theta}{h_e/H}+\frac{2}{\Lambda-1}\left(1+\frac{h'\cos\theta}{h_e/H}\right)^{-\Lambda+1}-\frac{2}{\Lambda-1}-\frac{1}{2\Lambda-1}\left(1+\frac{h'\cos\theta}{h_e/H}\right)^{-2\Lambda+1}+\frac{1}{2\Lambda-1}\right)\end{array}\right\}=0 \quad (44)$$

Eqs. (43) and (44) are nonlinear second-order transient partial differential equations. Utilizing the parameters from Table 1 [8,17] in Eqs. (43) and (44) we can obtain the height distributions for different incoming groundwater flow velocities and slope angles.

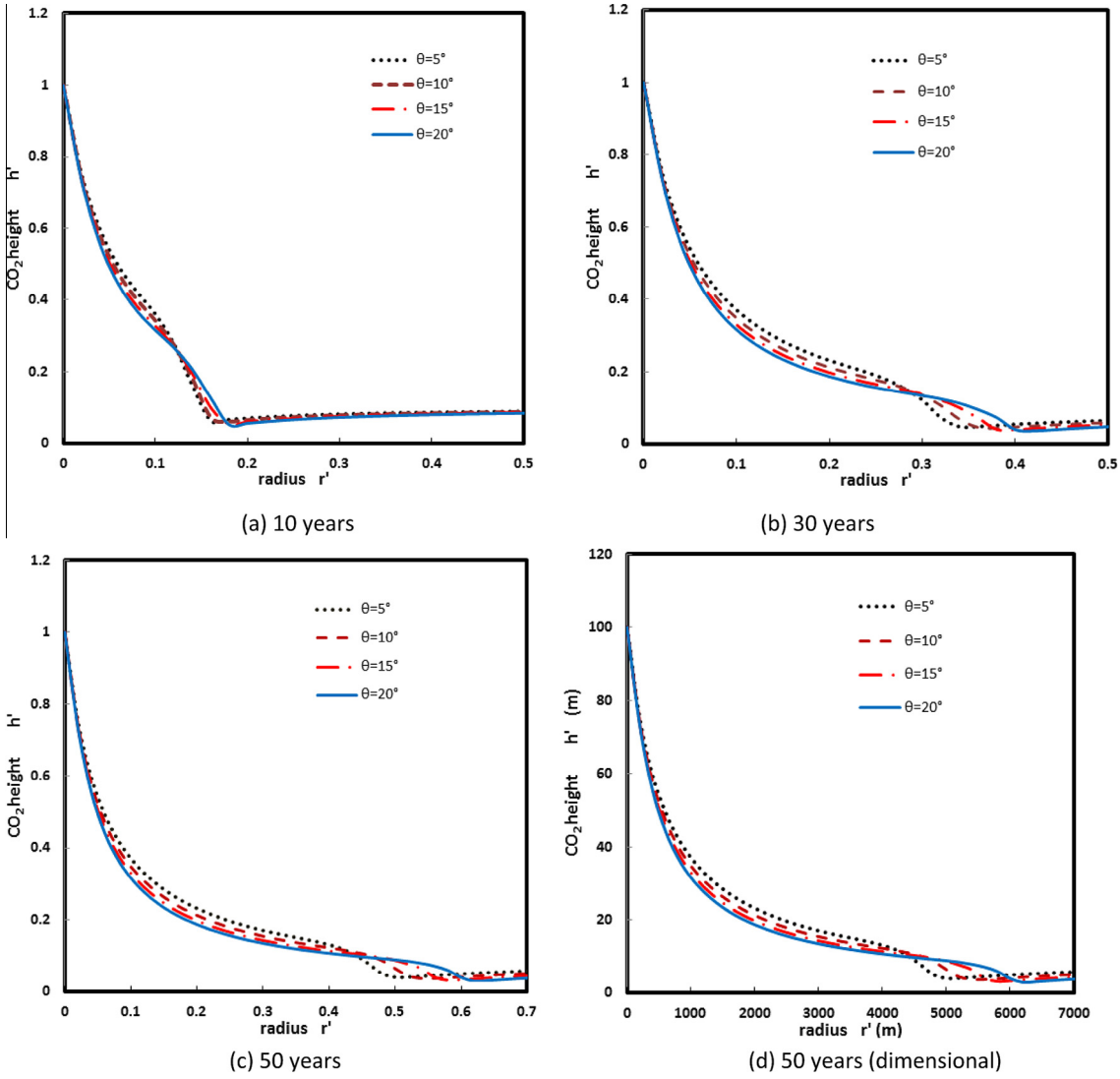

Fig. 6. Effect of the sloped stratum on the height distribution for an incoming groundwater flow of 0.1 ft/day after (a) 10 years (b) 30 years (c) 50 years (d) 50 years in dimensional form.

Table 2
Effect of the sloped stratum on the migration distance.

Angle	Years		
	10 years	30 years	50 years
	Distance (m)		
$\theta = 5°$	1550	3400	5000
$\theta = 10°$	1650	3600	5400
$\theta = 15°$	1750	3800	5800
$\theta = 20°$	1850	4000	6200

3. Results and discussion

3.1. Comparison with prior work

The results from our analysis is compared with the work of Norbotten and Celia [18] which is for the case without a slope and no incoming groundwater flow and is based on a sharp interface assumption. The comparison is shown for the limiting values used in their work and displayed in Fig. 5. It can be seen that there is excellent agreement between our analysis and their results for the limiting values used in their work. The difference between the results grows for latter years since we do account for the saturation transition zone. As such the results from our analysis show an increased penetration, as expected, for the latter years.

3.2. The up-dip side

By using Eq. (43), the height distribution under different slope angles and incoming ground water velocities can be analyzed. Three different slope angles 5°, 10°, 15°, 20° are chosen. As can be seen in Fig. 6, CO_2 migrates further for larger slopes. Since the density of CO_2 is less than that of the underground water, it stays on the upside of the underground water because of the buoyance

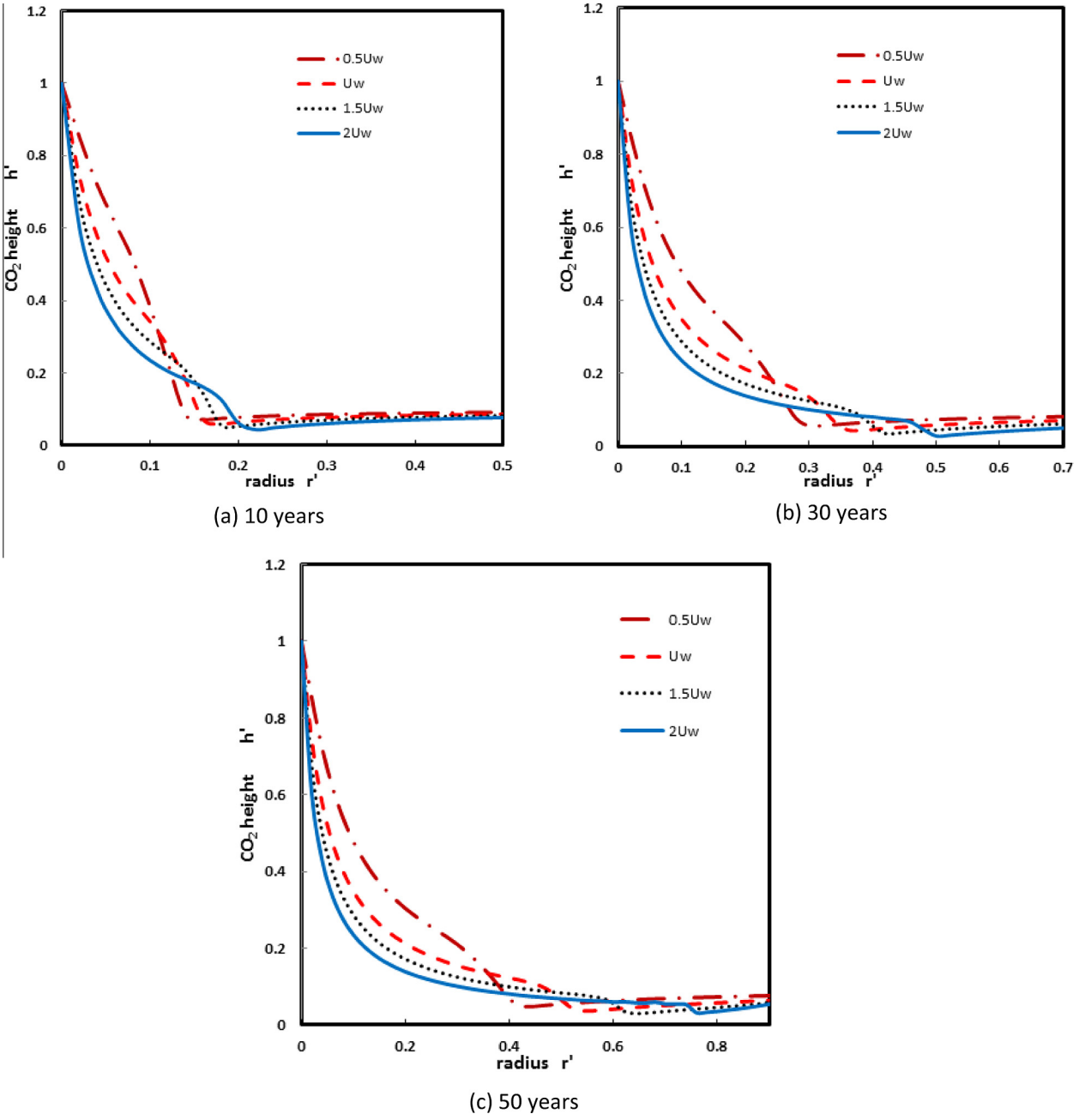

Fig. 7. Effect of the incoming groundwater on the height distribution for a sloped stratum ($\theta = 10°$), after (a)10 years, (b) 30 years, (c) 50 years.

Table 3
Effect of the incoming groundwater velocity on the migration distance.

Velocity	Years		
	10 years	30 years	50 years
	Distance (m)		
$0.5U_w$	1400	3000	4200
U_w	1550	3400	5000
$1.5U_w$	1800	4200	6200
$2U_w$	2200	5000	7600

force. For larger sloped angles, the height difference in the stratum increases. The buoyancy force will push CO_2 stream upwards. Thus CO_2 moves further for larger sloped angles. The height close to the injection point decreases due to the mass conservation. As can be seen in Fig. 6(a)–(c), the impact of a sloped stratum on the CO_2 height distribution becomes more apparent with time. Fig. 6(d) is the dimensional form of Fig. 6(c). It shows that the difference in the migration distance for CO_2 can reach over 1000 meters between sloped angles of 5° and 20° after 50 years. Table 2 displays the estimated migration distances for different sloped angles based on Fig. 6. It should be mentioned that the initial height is maintained for the regions where the injected CO_2 does not reach due to the sloped angle. The buoyancy causes the CO_2 in the occupied region to move upward. Thus, as the sloped angle increases, the height in this region decreases.

The impact of incoming underground water velocity on the CO_2 height distribution is displayed in Fig. 7, As expected, CO_2 migrates further with an increase in the incoming underground water velocity. Since the direction of CO_2 migration is the same as the flow direction, the underground water will help the CO_2 movement

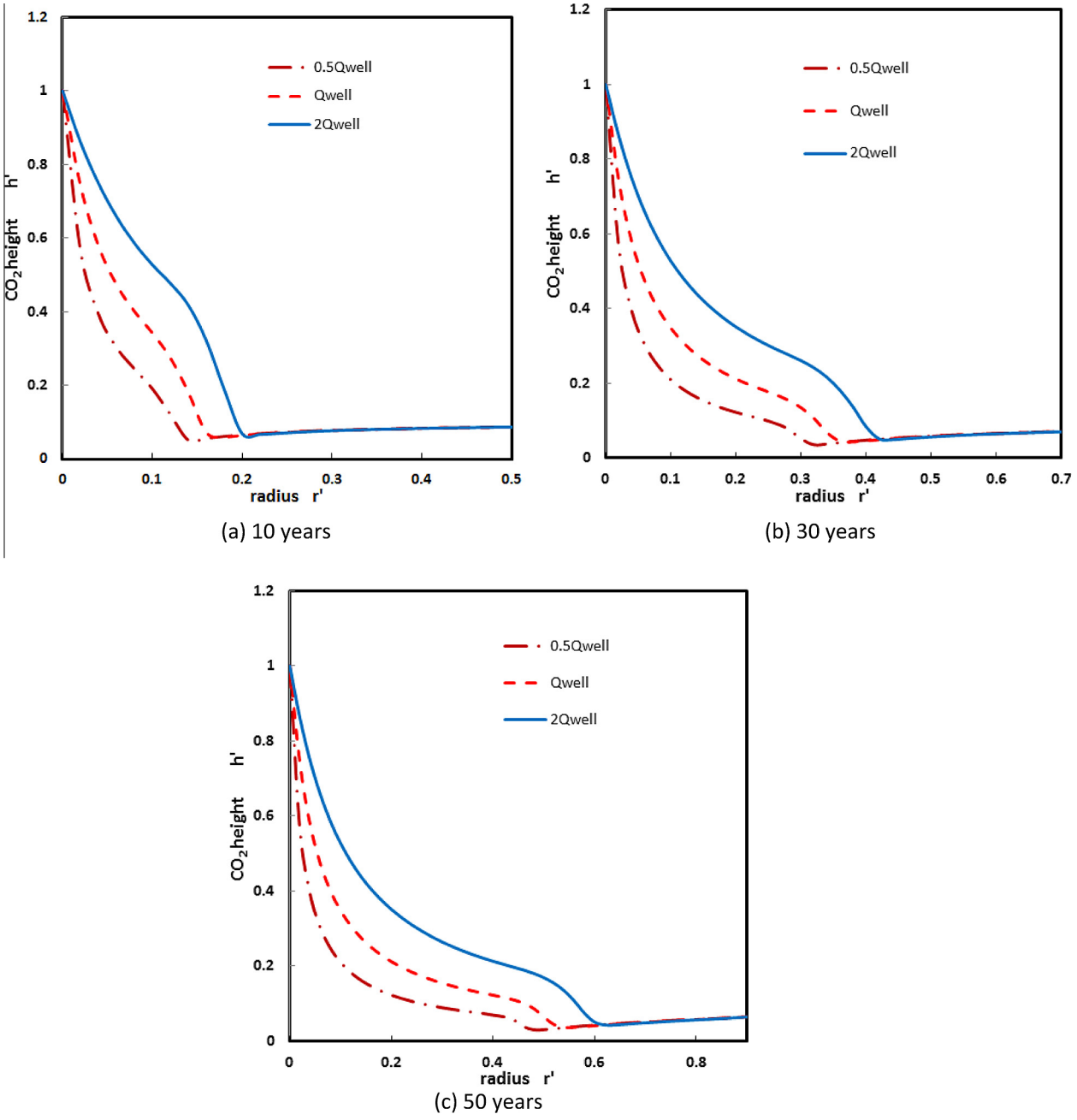

Fig. 8. Effect of the injection flow rate on the height distribution for a sloped stratum ($\theta = 10°$) and an incoming groundwater flow of 0.1ft/day after (a) 10 years, (b) 30 years, (c) 50 years.

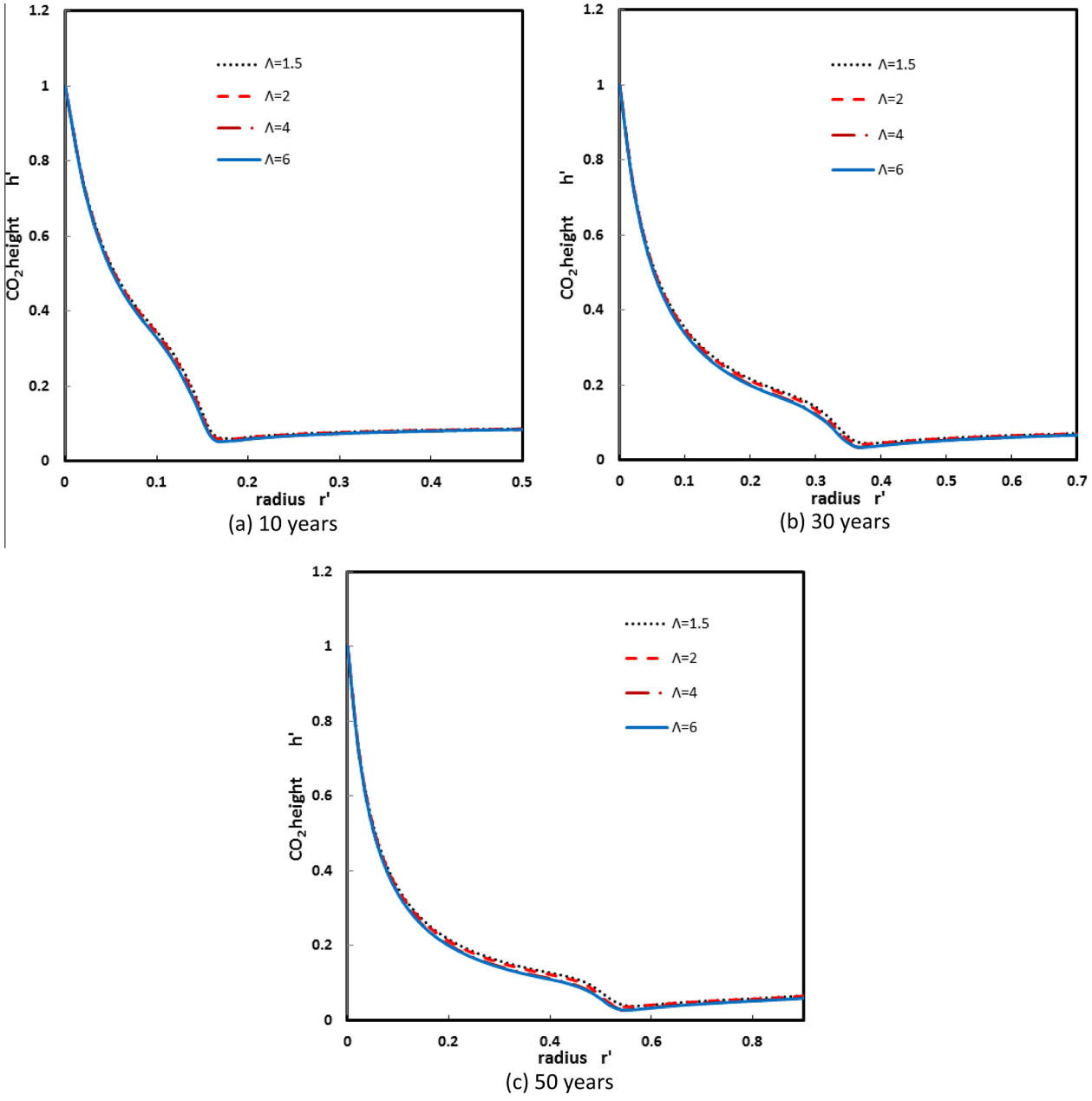

Fig. 9. Effect of pore size on the height distribution for a sloped stratum ($\theta = 10°$) and an incoming groundwater flow of 0.1ft/day after (a) 10 years, (b) 30 years, (c) 50 years.

due to the inertia and pressure. At the same time, due to the mass conservation, CO_2 height close to the injection point region decreases for larger incoming velocities since CO_2 migrates further. As seen in Fig. 7(a)–(c), the impact of incoming underground water velocity on the CO_2 height distribution becomes more apparent. Table 3 displays the estimated migration distances for different incoming groundwater velocities based on Fig. 7. For the region where injected CO_2 does not reach, the height will decrease with an increase in the flow rate of the incoming groundwater. The groundwater water pushes CO_2 forward due to pressure and buoyancy.

Fig. 8 shows the effect of the injection flow rate on the height distribution. As the injection flow rate increases, CO_2 will move further. For the region, which has not yet been affected by the injected CO_2 the height stays the same. Fig. 9 shows the effect of pore size on the height distribution, where Λ is a pore-size related parameter. The pores tend to be the same size with the growth of Λ. Thus increasing Λ will decrease the capillary pressure and capillary fringe. Based on Golding et al. [4] work, Λ = 1.5,2,4,6 are chosen to study the effect of pore size distribution. It shows that the height decreases with an increase in the pore size distribution index, Λ due to a decrease in the capillary fringe. However the effect is not significant especially for larger values of Λ. This shows that the capillary force does not have a substantial impact on the height distribution.

3.3. The down-dip side

The flow on the down-dip side is more complicated than the up-dip side. As r grows, the CO_2 velocity decreases. Since the CO_2 velocity is smaller than the incoming groundwater velocity, the groundwater flow will hinder the migration of CO_2. Thus for the down-dip side of the injection point, there should be a maximum migration distance, which depends on the incoming ground water velocity.

3.4. Critical Point

With the incoming groundwater velocity growing, we establish the existence of a critical velocity at which point CO_2 at the injection point will move only to the up-dip side. The critical point is governed by the following flux equations at the injection side. In this case, $Q_{wellL} = 0$ and $Q_{wellR} = Q_{well}$. Let's introduce a very small parameter, ε. As $r \to \varepsilon \Rightarrow \quad h' \to 1$.

On the up-dip side:

$$-\pi\frac{kk_{rn0}}{\mu_n}H^2\frac{h_e}{H\cos\theta}\left[\Delta\rho g\cos\theta r'\frac{\partial h'}{\partial r'}\frac{A}{A+B}-\Delta\rho g\sin\theta r'\frac{L}{H}\frac{A}{A+B}-\frac{1}{A+B}\frac{(Q_{well}+2qLr)}{\pi Hk}\right]$$
$$\left(\frac{h'\cos\theta}{h_e/H}+\frac{2}{\Lambda-1}\left(1+\frac{h'\cos\theta)}{h_e/H}\right)^{-\Lambda+1}-\frac{2}{\Lambda-1}-\frac{1}{2\Lambda-1}\left(1+\frac{h'\cos\theta}{h_e/H}\right)^{-2\Lambda+1}+\frac{1}{2\Lambda-1}\right)\Bigg|_{r=\varepsilon}=Q_{well} \tag{45}$$

On the down-dip side:

$$-\pi\frac{kk_{rn0}}{\mu_n}H^2\frac{h_e}{H\cos\theta}\left[\Delta\rho g\cos\theta r'\frac{\partial h'}{\partial r'}\frac{A}{A+B}+\Delta\rho g\sin\theta r'\frac{L}{H}\frac{A}{A+B}-\frac{1}{A+B}\frac{(-2qLr)}{\pi Hk}\right]$$
$$\left(\frac{h'\cos\theta}{h_e/H}+\frac{2}{\Lambda-1}\left(1+\frac{h'\cos\theta}{h_e/H}\right)^{-\Lambda+1}-\frac{2}{\Lambda-1}-\frac{1}{2\Lambda-1}(1+\frac{h'\cos\theta}{h_e/H})^{-2\Lambda+1}+\frac{1}{2\Lambda-1}\right)\Bigg|_{r=\varepsilon}=0 \tag{46}$$

Subtracting the above two cited fluxes will result

$$-\pi\frac{kk_{rn0}}{\mu_n}H^2\frac{h_e}{H\cos\theta}\left[-2\Delta\rho g\sin\theta r'\frac{L}{H}\frac{A}{A+B}-\frac{1}{A+B}\frac{(Q_{well}+4qLr)}{\pi Hk}\right]$$
$$\left(\frac{\cos\theta}{h_e/H}+\frac{2}{\Lambda-1}\left(1+\frac{\cos\theta)}{h_e/H}\right)^{-\Lambda+1}-\frac{2}{\Lambda-1}-\frac{1}{2\Lambda-1}\left(1+\frac{\cos\theta}{h_e/H}\right)^{-2\Lambda+1}+\frac{1}{2\Lambda-1}\right)\Bigg|_{r=\varepsilon}=Q_{well} \tag{47}$$

Utilizing Eqs. (41) and (42) and parameter values in Table 1 in Eq. (47) we will obtain the groundwater velocity at the critical point as

$$U_{wc} = (0.004Q_{well}/\varepsilon - 0.00221)/398.4 \tag{48}$$

For example, for a stratum characteristic length of L = 10,000m, and taking $\varepsilon = 10^{-6}$, we obtain the groundwater velocity at the critical point as U_{wc} = 0.44m/s.

Only when the asymmetrical distribution is taken into account, it will lead to the existence of critical point and velocity. This is indeed the case here because we have taken into account the asymmetrical nature of the flow field.

4. Conclusions

A comprehensive analysis for migration and injection of CO_2 in a sloped aquifer is presented in this work. The impact of the sloped angle and groundwater flow on the height distribution is established. The saturation transition zone along with capillary forces is taken into account in our analysis. A comprehensive model is developed to describe CO_2 migration under these conditions. The asymmetrical distribution is incorporated in the analysis presented in this work. The height h we have solved for is the average height over all angles ψ on the down-dip or the up-dip side for any specific radius r. The transition zone increases the CO_2 height distribution to some extent. In the limiting case of no incoming groundwater, no sloped stratum and negligible transition zone, our results match very well with a prior work in this area. The present analysis provides a more exact and effective solution for the long duration injection. The CO_2 on the up-dip side moves further than the down-dip side, which must be incorporated in evaluating the reservoir capacity. For a stratum with a sloped angle, CO_2 will migrate further in the upper side of CO_2 injection point. The incoming underground water helps CO_2 move further on the up-dip side of CO_2 injection point where CO_2 flow direction is the same as the incoming underground water. The existence of a critical velocity when the incoming CO_2 at the injection point will only move to the up-dip side was established. The presented analysis for the first time incorporates the injection velocity, the saturation transition zone and the sloped incoming ground water flow.

Conflict of Interest

None declared.

Acknowledgments

This work was supported in part by the U.S. Department of Energy. The support was provided by Lawrence Berkeley National Laboratory (Berkeley Lab) through the U.S. Department of Energy Contract No. DE-AC02-05CH11231.

References

[1] S. Bachu, W.D. Gunter, E.H. Perkins, Aquifer disposal of CO_2: hydrodynamic and mineral trapping, Energy Convers. Manage. 35 (4) (1994) 269–279.
[2] C.W. Macminn, M.L. Szulczewski, R. Juanes, CO_2 migration in saline aquifers. Part 1. Capillary trapping under slope and groundwater flow, J. Fluid Mech. 662 (2010) 329–351.
[3] M.A. Hesse, F.M. Orr Jr., H.A. Tchelepi, Gravity currents with residual trapping, J. Fluid Mech. 611 (2008) 35–60.
[4] M.J. Golding, J.A. Neufeld, M.A. Hesse, H.E. Huppert, Two-phase gravity currents in porous media, J. Fluid Mech. 678 (2011) 248–270.
[5] B. Metz, O. Davidson, H. de Coninck, M. Loos, L. Meyer (Eds.), 2005 IPCC Special Report on Carbon Dioxide Capture and Storage, Cambridge University Press, 2005. prepared by Working Group III of the Intergovernmental Panel on Climate Change.
[6] V. Srinivasan, K. Vafai, Analysis of linear encroachment in two-immiscible fluid systems in a porous medium, ASME J. Fluids Eng. 116 (1994) 135–139.
[7] K. Vafai, B. Alazmi, On the linear encroachment in two-immiscible fluid systems in a porous medium, ASME J. Fluids Eng. 125 (2003) 738–739.
[8] J.M. Nordbotten, M.A. Celia, An improved analytical solution for interface upconing around a well, Water Resour. Res. 42 (8) (2006) W08433.
[9] M.J. Golding, H.E. Huppert, J.A. Neufeld, The effects of capillary forces on the axisymmetric propagation of two-phase, constant-flux gravity currents in porous media, Phys. Fluids 25 (3) (2013) 036602.
[10] J.M. Nordbotten, H.K. Dahle, Impact of the capillary fringe in vertically integrated models for CO2 storage, Water Resour. Res. 47 (2011) W02537.
[11] J.M. Nordbotten, M.A. Celia, Geological Storage of CO2: Modeling Approaches for Large-Scale Simulation, John Wiley and Sons, Ltd, 2011, ISBN 9780470889466. 256 pp.
[12] J.M. Nordbotten, B. Flemisch, S.E. Gasda, H.M. Nilsen, Y. Fan, G.E. Pickup, B. Wiese, M.A. Celia, H.K. Dahle, G.T. Eigestad, K. Pruess, Uncertainties in practical simulation of CO2 storage, Int. J. Greenhouse Gas Control 9 (2012) 234–242.
[13] B. Court, K.W. Bandilla, M.A. Celia, A. Janzen, M. Dobossy, J.M. Nordbotten, Applicability of vertical-equilibrium and sharp-interface assumptions in CO_2 sequestration modeling, Int. J. Greenhouse Gas Control 10 (2012) 134–147.
[14] R.J. Brooks, A.T. Corey, Hydraulic properties of porous media, Hydrol. Pap. 3, Colo. State Univ., Fort Collins, 1964.
[15] A.T. Corey, The interrelation between gas and oil relative permeabilities, Prod. Monthly 19 (1) (1954) 38–41.
[16] B. Bennion, S. Bachu, 2005. Relative permeability characteristics for supercritical CO_2 displacing water in a variety of potential sequestration zones in the western Canada sedimentary basin. in: SPE Annual Technical Conference and Exhibition, Dallas, Texas, October 9–12. SPE 95547.
[17] J.M. Nordbotten, M.A. Celia, Geological Storage of CO_2 – Modeling Approaches for Large-scale Simulation, John Wiley & Sons, 2012, ISBN 978-0-470-88946-6.
[18] J.M. Nordbotten, M.A. Celia, Similarity solutions for fluid injection into confined aquifers, J. Fluid Mech. 561 (2006) 307–327.